Monthly Notices
of the
ROYAL ASTRONOMICAL SOCIETY

Mon. Not. R. Astron. Soc. **417,** 333–347 (2011) doi:10.1111/j.1365-2966.2011.19266.x

Creation of cosmic structure in the complex galaxy cluster merger Abell 2744

J. Merten,[1,2]★† D. Coe,[3]★ R. Dupke,[4,5,6] R. Massey,[7] A. Zitrin,[8] E. S. Cypriano,[9] N. Okabe,[10] B. Frye,[11] F. G. Braglia,[12] Y. Jiménez-Teja,[13] N. Benítez,[13] T. Broadhurst,[14,15] J. Rhodes,[16,17] M. Meneghetti,[2] L. A. Moustakas,[17] L. Sodré Jr,[9] J. Krick[18] and J. N. Bregman[4]

[1]*Institut für Theoretische Astrophysik, ZAH, Albert-Ueberle-Straße 2, 69120 Heidelberg, Germany*
[2]*INAF–Osservatorio Astronomico di Bologna, Via Ranzani 1, 40127 Bologna, Italy*
[3]*Space Telescope Science Institute, Baltimore, MD 21218, USA*
[4]*University of Michigan, Ann Arbor, MI 48109-1090, USA*
[5]*Eureka Scientific, 2452 Delmer Street 100, Oakland, CA 94602-3017, USA*
[6]*Observatório Nacional, Rua General José Cristino 77, Rio de Janeiro, 20921-400, Brazil*
[7]*University of Edinburgh, Royal Observatory, Blackford Hill, Edinburgh EH9 3HJ*
[8]*School of Physics and Astronomy, Raymond and Beverly Sackler Faculty of Exact Sciences, Tel Aviv University, Tel Aviv 69978, Israel*
[9]*Instituto de Astronomia, Geofísica e Ciências Atmosfericos, Universidade de São Paulo (IAG/USP), 05508-090 São Paulo/SP, Brazil*
[10]*Academia Sinica Institute of Astronomy and Astrophysics (ASIAA), PO Box 23-141, Taipei 10617, Taiwan*
[11]*Department of Physics and Astronomy, 2130 Fulton Street, University of San Francisco, San Francisco, CA 94117, USA*
[12]*Department of Physics and Astronomy, University of British Columbia, 6224 Agricultural Road, Vancouver, BC V6T 1Z1, Canada*
[13]*Instituto de Astrofísica de Andalucía (CSIC), C/Camino Bajo de Huétor 24, Granada 18008, Spain*
[14]*Department of Theoretical Physics, University of Basque Country UPV/EHU, Leioa, Spain*
[15]*IKERBASQUE, Basque Foundation for Science, 48011 Bilbao, Spain*
[16]*Jet Propulsion Laboratory, California Institute of Technology, 4800 Oak Grove Drive, MS 169-327, Pasadena, CA 91109, USA*
[17]*California Institute of Technology, 1201 East California Boulevard, Pasadena, CA 91125, USA*
[18]*Spitzer Science Center, MS 220-6, California Institute of Technology, Pasadena, CA 91125, USA*

Accepted 2011 June 15. Received 2011 June 14; in original form 2011 March 15

ABSTRACT

We present a detailed strong-lensing, weak-lensing and X-ray analysis of Abell 2744 ($z = 0.308$), one of the most actively merging galaxy clusters known. It appears to have unleashed 'dark', 'ghost', 'bullet' and 'stripped' substructures, each $\sim 10^{14}\,\mathrm{M}_{\odot}$. The phenomenology is complex and will present a challenge for numerical simulations to reproduce. With new, multiband *Hubble Space Telescope* (*HST*) imaging, we identify 34 strongly lensed images of 11 galaxies around the massive Southern 'core'. Combining this with weak-lensing data from *HST*, VLT and Subaru, we produce the most detailed mass map of this cluster to date. We also perform an independent analysis of archival *Chandra* X-ray imaging. Our analyses support a recent claim that the Southern core and Northwestern substructure are post-merger and exhibit morphology similar to the Bullet Cluster viewed from an angle. From the separation between X-ray emitting gas and lensing mass in the Southern core, we derive a new and independent constraint on the self-interaction cross-section of dark matter particles $\sigma/m < 3 \pm 1\,\mathrm{cm}^2\,\mathrm{g}^{-1}$. In the Northwestern substructure, the gas, dark matter and galaxy components have become separated by much larger distances. Most curiously, the 'ghost' clump (primarily gas) *leads* the 'dark' clump (primarily dark matter) by more than 150 kpc. We propose an enhanced 'ram-pressure slingshot' scenario which may have yielded this reversal of components with such a large separation, but needs further confirmation by follow-up observations and numerical simulations. A secondary merger involves a second

★Both authors contributed equally to this work.
†E-mail: jmerten@ita.uni-heidelberg.de

'bullet' clump in the North and an extremely 'stripped' clump to the West. The latter appears to exhibit the largest separation between dark matter and X-ray emitting baryons detected to date in our sky.

Key words: gravitational lensing: strong – gravitational lensing: weak – galaxies: clusters: individual: Abell 2744 – dark matter – large-scale structure of Universe – X-rays: individual: Abell 2744.

1 INTRODUCTION

The standard Λcold dark matter (ΛCDM) cosmological model suggests a bottom-up sequence of structure formation, in which a series of merging events culminate in massive clusters of galaxies, the latest structures to form in the observable Universe (Bond et al. 1991; Lacey & Cole 1993). The number of clusters as a function of their mass (the steep, high end of the mass function) depends sensitively upon cosmological parameters (e.g. Vikhlinin et al. 2009) and has become an important observational test of cosmology. Most measurements of cluster masses rely upon the calibration of more easily observable proxies, such as X-ray luminosity, temperature or galaxy richness. However, clusters form through multiple, dynamic accretions, so are likely to be turbulent places, and the turmoil affects those observable proxies. It is therefore vital to quantitatively understand the merging process, for example by mapping the distribution of dark matter, stars and baryonic gas in systems at many different stages of the merger.

Merging clusters of galaxies have become useful laboratories in which to study the nature and interaction properties of dark matter. The best-studied example is the Bullet Cluster 1ES 0657–558 ($z = 0.296$) (Tucker et al. 1998; Markevitch et al. 2002). Combined X-ray and gravitational lensing analyses show a clear separation between the centres of X-ray emission and the peaks in surface mass density – indicating a fundamental difference between baryonic gas, which feels the pressure of the collision, and dark matter, which is nearly collisionless (Clowe, Gonzalez & Markevitch 2004; Bradač et al. 2006; Clowe et al. 2006). The discovery and interpretation of the Bullet Cluster have inspired a lively debate about whether such a system could exist in different cosmological models (see e.g. Hayashi & White 2006). Improvements are continuing in numerical simulations (Milosavljević et al. 2007; Springel & Farrar 2007; Mastropietro & Burkert 2008; Lee & Komatsu 2010). Observations have also broadened, with discoveries of a possible line-of-sight merger CL0024+1654 (Czoske et al. 2002; Hoekstra 2007; Jee et al. 2007b; Zitrin et al. 2009; Umetsu et al. 2010; Zu Hone et al. 2009b; Zu Hone, Lamb & Ricker 2009a), and other systems including the Baby Bullet (MACS J0025.4−1222) (Bradač et al. 2008), the Cosmic Train Wreck (Abell 520) (Mahdavi et al. 2007; Okabe & Umetsu 2008), Abell 2146 (Russell et al. 2010), Abell 521 (Giacintucci et al. 2008; Okabe et al. 2010a) and Abell 3667 (Finoguenov et al. 2010). All these systems place potentially tight constraints on the interaction between baryons and dark matter, and are exemplary probes for our understanding of structure formation within gravitationally bound systems.

In the archival data of 38 merging clusters, Shan et al. (2010) found the largest offset between X-ray and lensing signals to occur in the massive ($L_X = 3.1 \times 10^{45}$ erg s^{-1} in the 2–10 keV range; Allen 1998) cluster Abell 2744 (also known as AC118, or RXCJ0014.3−3022) at a redshift of $z = 0.308$ (Couch & Newell 1984). The ∼250 kpc offset is larger than that in the Bullet Cluster – although, as we shall discuss later, this value does not describe the separation of the main mass clump from its stripped gas component. Nevertheless, Abell 2744 is undergoing a particularly interesting merger. The complex interplay between multiple dark matter and baryonic components appears to have unleashed 'ghost', 'dark', 'stripped' and 'bullet' clusters.

The first hint that Abell 2744 is in the middle of a major merging event arose from observation of a powerful and extended radio halo [$P(1.4\,\mathrm{GHz}) > 1.6 \times 10^{36}$ Watt; Giovannini, Tordi & Feretti 1999; Govoni et al. 2001a,b]. This indicated the presence of relativistic electrons accelerated through high Mach shocks or turbulence (e.g. Sarazin 2004). The picture was clarified by X-ray studies (Kempner & David 2004; Zhang et al. 2004) that revealed substructure near the cluster core, plus an additional luminous structure towards the Northwest. Kinematic observations of cluster member galaxies (Girardi & Mezzetti 2001) suggested a bimodal distribution in redshift space, but were not at first considered significant. Recent kinematic studies focusing solely on Abell 2744 definitely show a bimodal velocity dispersion in the cluster centre, together with a third group of cluster members near the Northwestern X-ray peak (Boschin et al. 2006; Braglia et al. 2009). Although there is no evidence for non-thermal X-ray emission (Million & Allen 2009), the fraction of blue star-forming galaxies (Braglia, Pierini & Böhringer 2007, and references therein) also seems to be enhanced. A default explanation emerged for the centre of Abell 2744, featuring a major merger in the North–South direction with a small inclination towards the line of sight and a ∼3:1 mass ratio of the merging entities (Kempner & David 2004; Boschin et al. 2006). More controversial is the role of the Northwestern structure. Kempner & David (2004) detected a cold front on its SW edge and a possible shock front towards the cluster core, and so concluded that it is falling towards the main mass. More recent analysis of *Chandra* data (Owers et al. 2011) failed to confirm the presence of the shock front, only a cold front towards the Northern edge, and the authors proposed that the structure is moving instead towards the North/Northeast, after being deflected from the main cluster in an off-centre core passage. What seems sure is that we are at least observing a complicated merger between three separate bodies (Braglia et al. 2007).

Until now, Abell 2744 has been better constrained from X-ray and kinematic studies than by gravitational lensing. So far, Smail et al. (1997) detected a weak-lensing signal and strong-lensing features, followed by Allen (1998) who found a large discrepancy in the mass estimates for Abell 2744 from X-ray and strong-lensing reconstructions. Given the cluster's dynamical state, this finding is perhaps no longer surprising since the merging would induce non-thermal support and elongation along the line of sight, which increases the systematics from both methods. The most recent weak-lensing analysis (Cypriano et al. 2004) showed indications of substructure in the reconstructed surface mass density, but did not reach the resolution required for more quantitative statements. Here, we present the results of a *Hubble Space Telescope* (*HST*) imaging

survey, aimed at clarifying the evolutionary stage of this complex system.

This article is organized as follows. In Section 2 we present our comprehensive lensing analysis, mainly based on newly acquired data taken with the Advanced Camera for Surveys (ACS) on the *HST*. In Section 3, we describe a complementary X-ray analysis based on *Chandra* data. We discuss cosmological implications and an interpretation of the merging scenario in Section 4, and we conclude in Section 5. Throughout this paper we assume a cosmological model with $\Omega_{\rm m} = 0.3$, $\Omega_\Lambda = 0.7$ and $h = 0.7$. At the cluster's redshift $z = 0.308$, 1 arcsec corresponds to 4.536 kpc.

2 LENSING ANALYSIS

Our recently acquired, multiband *HST*/ACS imaging enables us to significantly improve upon previous mass models of Abell 2744. Using the parametric method described in Section 2.2, we have identified strong gravitational lensing of 11 background galaxies producing 34 multiple images around the Southern core, with an Einstein radius of $r_{\rm E} \sim 30$ arcsec (see below). These enable us to tightly constrain the position and shape of the core mass distribution. No such multiple-image systems are revealed around the N or NW clumps, immediately indicating that their masses are lower. Our *HST* images also yield ∼62 galaxies arcmin^{-2} for weak-lensing analysis [after charge transfer inefficiency (CTI) corrections are performed, as described below]. This enables detailed mass modelling throughout our *HST* field of view. To probe the cluster merger on even larger scales, we incorporate ground-based weak-lensing measurements from VLT and Subaru.

We simultaneously fit all of these strong- and weak-lensing observations using our well-tested mass reconstruction algorithm (Merten et al. 2009; Meneghetti et al. 2010a) [which is similar to that used by Bradač et al. (2006) and Bradač et al. (2008) to map the Bullet Cluster and the Baby Bullet]. Importantly, we make no assumptions about mass tracing light in the combined analysis. It should be noted though that we rely on a parametric method, assuming that light traces mass, to identify multiple-image systems. We account for possible uncertainties in this identification, by resampling the set of less confident identifications in the errors analysis based on a bootstrapping technique (see Section 2.4). Our analysis reveals *four* individual clumps of mass $\gtrsim 10^{14}\,{\rm M}_\odot$ within a 250 kpc radius. Previous weak-lensing analysis of VLT images alone had resolved but a single broad mass clump (Cypriano et al. 2004). Below we describe our data sets, analyses and results in more detail. The central cluster field and a preview on the matter and gas distribution are presented in Fig. 1, which also shows the contours encircling different areas of specific probability, that a mass peak is located at this specific location of the reconstructed field.

2.1 The *HST*/ACS data set

The *HST* data consist of two pointings in Cycle 17 (data taken between 2009 October 27 and 30; Proposal ID: 11689, P.I.: R. Dupke) with ∼50 per cent overlap between the pointings. The images were taken with the ACS/WFC camera using three different filters, F435W (16.2 ks[1]), F606W (13.3 ks) and F814W (13.2 ks).

The *HST*/ACS camera had been in orbit for 8 years when the imaging was acquired. During this time above the protection of the Earth's atmosphere, its CCD detectors had been irreparably damaged by a bombardment of high-energy particles. During CCD readout, photoelectrons are transported to the readout amplifier through a silicon lattice. Damage to this lattice creates charge traps that delay some electrons and spuriously trail the image – in a way that alters the shapes of galaxies more than the gravitational lensing signal that we are trying to measure. To undo this trailing and correct the `_raw` images pixel-by-pixel, we used the detector readout model of Massey et al. (2010), updated for device performance post Servicing Mission 4 by Massey (2010). The corrected data were then reduced via the standard CALACS pipeline (Pavlovsky 2006), and stacked using multidrizzle (Koekemoer et al. 2002).

2.2 Strong lensing

We concentrate our strong-lensing analysis on the reduced ACS images only. Several strong-lensing features are immediately identifiable by eye on the combined three-band image (Fig. 2). To find additional multiple images across the field of view, we apply the well-tested approach of Zitrin et al. (2009) (see also Zitrin et al. 2011b) to lens modelling, which has previously uncovered large numbers of multiply-lensed galaxies in ACS images of Abell 1689, Cl0024, 12 high-z MACS clusters, MS1358 and Abell 383 (respectively, Broadhurst et al. 2005; Zitrin et al. 2009, 2010, 2011a,c,d).

In the Zitrin et al. (2009) method, the large-scale distribution of cluster mass is approximated by assigning a power-law mass profile to each galaxy, the sum of which is then smoothed. The degree of smoothing (S) and the index of the power law (q) are the most important free parameters determining the mass profile. A worthwhile improvement in fitting the location of the lensed images is generally found by expanding to first order the gravitational potential of this smooth component, equivalent to a coherent shear describing the overall matter ellipticity, where the direction of the shear and its amplitude are free parameters. This allows for some flexibility in the relation between the distribution of dark matter and the distribution of galaxies, which cannot be expected to trace each other in detail. The total deflection field $\boldsymbol{\alpha}_{\rm T}(\boldsymbol{\theta})$ consists of the galaxy component, $\boldsymbol{\alpha}_{\rm gal}(\boldsymbol{\theta})$, scaled by a factor $K_{\rm gal}$, the cluster dark matter component $\boldsymbol{\alpha}_{\rm DM}(\boldsymbol{\theta})$, scaled by $(1 - K_{\rm gal})$, and the external shear component $\boldsymbol{\alpha}_{\rm ex}(\boldsymbol{\theta})$:

$$\boldsymbol{\alpha}_{\rm T}(\boldsymbol{\theta}) = K_{\rm gal}\boldsymbol{\alpha}_{\rm gal}(\boldsymbol{\theta}) + (1 - K_{\rm gal})\boldsymbol{\alpha}_{\rm DM}(\boldsymbol{\theta}) + \boldsymbol{\alpha}_{\rm ex}(\boldsymbol{\theta}), \quad (1)$$

where the deflection field at position $\boldsymbol{\theta}_m$ due to the external shear, $\boldsymbol{\alpha}_{\rm ex}(\boldsymbol{\theta}_m) = (\alpha_{{\rm ex},x}, \alpha_{{\rm ex},y})$, is given by

$$\alpha_{{\rm ex},x}(\boldsymbol{\theta}_m) = |\gamma|\cos(2\phi_\gamma)\Delta x_m + |\gamma|\sin(2\phi_\gamma)\Delta y_m, \quad (2)$$

$$\alpha_{{\rm ex},y}(\boldsymbol{\theta}_m) = |\gamma|\sin(2\phi_\gamma)\Delta x_m - |\gamma|\cos(2\phi_\gamma)\Delta y_m, \quad (3)$$

where $(\Delta x_m,\ \Delta y_m)$ is the displacement vector of the position $\boldsymbol{\theta}_m$ with respect to a fiducial reference position, which we take as the lower-left pixel position (1, 1), and ϕ_γ is the position angle of the spin-2 external gravitational shear measured anti-clockwise from the x-axis. The normalization of the model and the relative scaling of the smooth dark matter component versus the galaxy contribution bring the total number of free parameters in the model to six. This approach to strong lensing is sufficient to accurately predict the locations and internal structure of multiple images, since in practice the number of multiple images readily exceeds the number of free parameters, which become fully constrained.

Two of the six free parameters, namely the galaxy power-law index q and the smoothing degree S, can be initially set to reasonable values so that only four of the free parameters need to be

[1] Equally split between the two pointings.

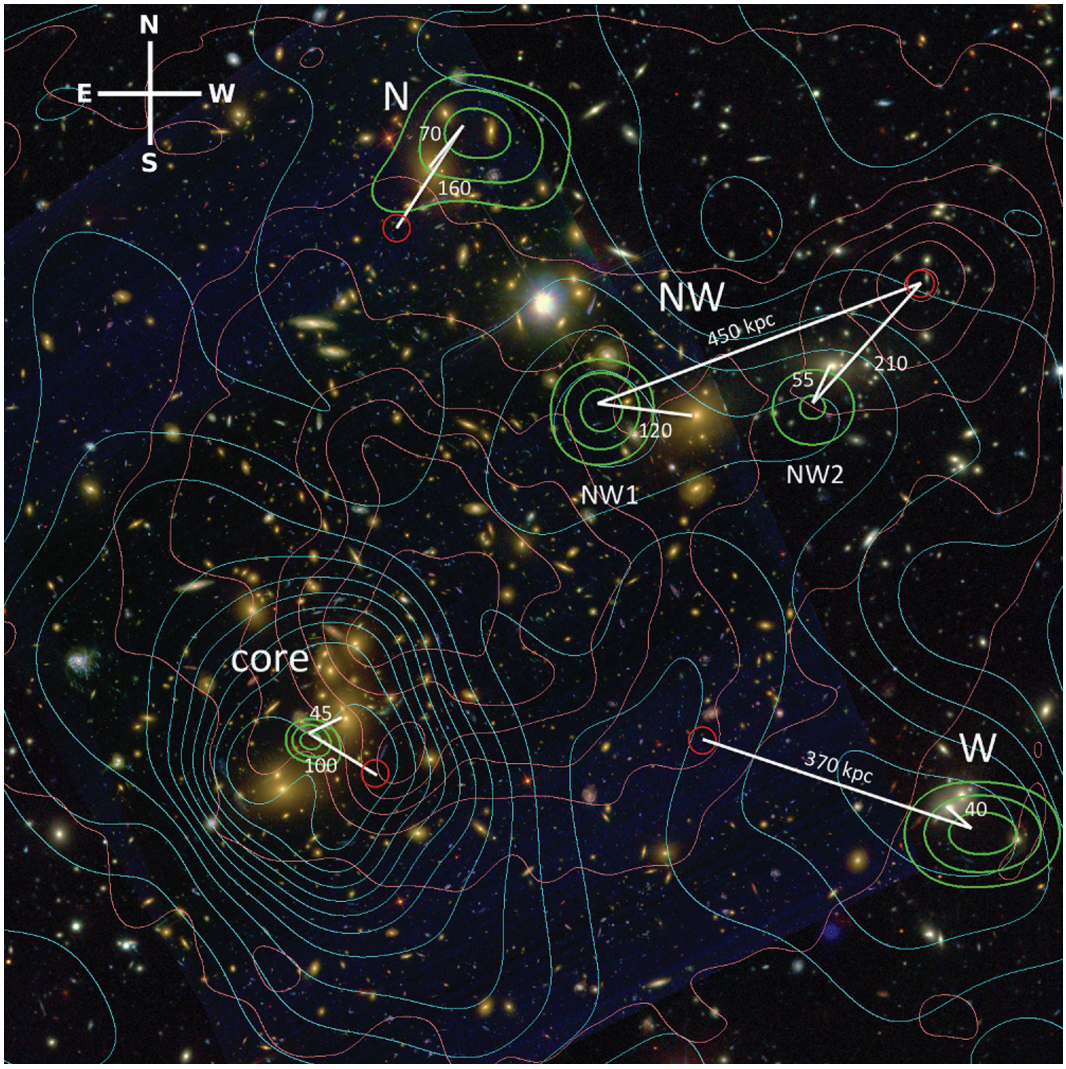

Figure 1. The field of Abell 2744, with different interesting features. The false-colour background is provided by *HST*/ACS (the two pointings can be identified by the higher, blue background noise level), VLT and Subaru images on a field size of 240 × 240 arcsec^2 (∼1.1 Mpc on a side). Overlaid in cyan are the surface mass density contours most concentrated in the 'core' area and in magenta the more evenly distributed X-ray luminosity contours. The peak positions of the core, N, NW and W clumps are indicated by the green likelihood contours, derived from the bootstrap samples. Contours are 86 per cent, 61 per cent and 37 per cent of the peak likelihood for each clump. (Assuming a Gaussian probability distribution, these would correspond to 0.3σ, 1σ and 2σ confidence contours.) Note that the NW clump most likely peaks in the area indicated by NW1 (in 95 per cent of the bootstrap realizations), but peaks also at NW2 in 54 per cent of the bootstrap realizations. The small red circles show the position of the local overdensities in the gas distribution, associated with each individual dark matter clump. The white rulers show the separation between dark matter peaks and the bright clusters galaxies and local gas peaks.

fitted at first. This sets a very reliable starting point using obvious systems. The mass distribution is therefore well-constrained and uncovers many multiple images that can be iteratively incorporated into the model, by using their redshift estimation, from photometry, spectroscopy or model prediction and location in the image plane. At each stage of the iteration, we use the model to lens the most obvious lensed galaxies back to the source plane by subtracting the derived deflection field, then relens the source plane to predict the detailed appearance and location of additional counter images, which may then be identified in the data by morphology, internal structure and colour. We stress that multiple images found this way must be accurately reproduced by our model and are not simply eyeball 'candidates' requiring redshift verification. The best fit is assessed by the minimum rms uncertainty in the image plane

$$rms^2_{\rm images} = \sum_i ((x_i' - x_i)^2 + (y_i' - y_i)^2)/N_{\rm images}, \quad (4)$$

where x_i' and y_i' are the locations given by the model, x_i and y_i are the real image locations, and the sum is over the total number of images $N_{\rm images}$. The best-fitting solution is unique in this context, and the model uncertainty is determined by the locations of predicted images in the image plane. Importantly, this image-plane minimization does not suffer from the well-known bias involved with source plane minimization, where solutions are biased by minimal scatter towards shallow mass profiles with correspondingly higher magnification.

In Abell 2744 we have uncovered a total number of 34 multiple images belonging to 11 background sources. We label the different systems in Fig. 2, which also shows the critical curve of the cluster derived from the strong-lensing model. The model predicts an Einstein radius of $r_{\rm E} = 30 \pm 3$ arcsec. With such a large number of clear multiple images we can constrain the inner mass distribution very well, and we shall incorporate these

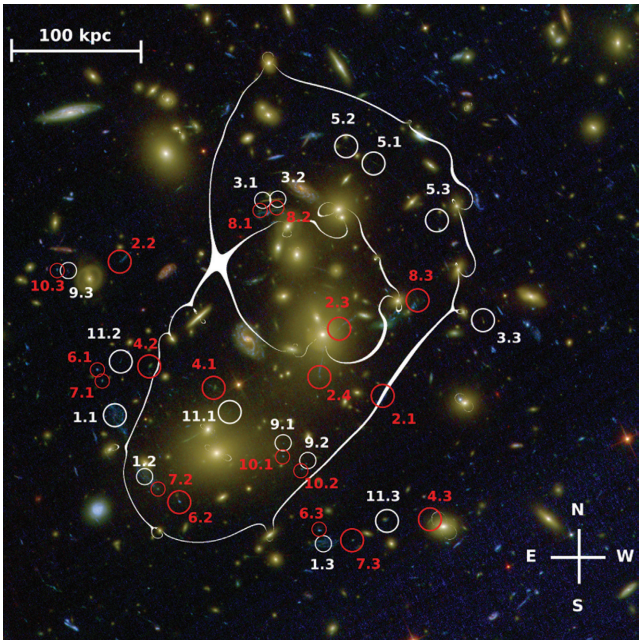

Figure 2. A zoom into the innermost core region of the *HST*/ACS images. Shown as a continuous white line is the critical curve of the cluster as it is derived from the strong-lensing model. It assumes a source redshift $z_s = 2.0$. Also shown are the approximate positions of the identified multiple-image systems as they are listed in Table 1 with a varying two-colour scheme to avoid confusion of close-by images. These systems were found by the method of Zitrin et al. (2009) and are not simple optical identifications. The visible field size is $\sim$100 $\times$ 100 arcsec^2, translating to $\sim$450 kpc on a side.

constraints into our joint strong- and weak-lensing analysis described in Section 2.4.

2.3 Weak lensing

Several areas outside the cluster core are of special interest, due to the complicated structure of this merging cluster. We measure the shapes of background galaxies to derive a weak-lensing signal and extend our mass reconstruction over a much larger field. Since our *HST* data cover only a limited field of view, we also include VLT and Subaru imaging in our weak-lensing analysis. Additional *HST* pointings in the future are crucial for a full interpretation of this merger, as we shall discuss in the course of this analysis.

2.3.1 HST/ACS

To select lensed background galaxies, we obtained photometric redshifts based on our three filters using Bayesian photometric redshifts (BPZ) (Benítez 2000; Coe et al. 2006). Cluster ellipticals at $z \sim 0.3$ occupy a unique region in our colour–colour space, enabling us to obtain better than expected results.

Of the 118 galaxies with published spectroscopic redshifts (Owers et al. 2011 and references therein; all $z < 0.7$) within our field of view, 99 yield confident photo-zs, accurate to $\Delta z \sim 0.06\,(1 + z)$ rms with no significant outliers. Background galaxies were selected as those with confident photo-$z > 0.5$. This cut successfully excludes all five foreground and 86 cluster galaxies in our spec-z sample with confident photo-z (though one cluster galaxy was assigned a less confident photo-$z \sim 0.8$). However, given our limited photometric coverage, we do not rule out some contamination of our background sample with foreground and/or cluster galaxies.

We measure the weak gravitational lensing signal in the F814W *HST* exposures, which are the deepest and contain the most galaxies at high redshift. We measure their shapes, and correct them for convolution by the point spread function (PSF), using the 'RRG' (Rhodes, Refregier & Groth 2000) pipeline developed for the *HST* COSMOS survey (Leauthaud et al. 2007; Massey et al. 2007). The RRG method is particularly optimized for use on high-resolution, space-based data. Since *HST* expands and contracts as it warms in the Sun or passes through the shadow of the Earth, even this telescope does not have a constant PSF. However, 97 per cent of the variation in its PSF can be accounted for by variation in its focal length (Jee et al. 2007a, the separation between the primary and secondary mirrors). We therefore measure its focal length by matching the shapes of the $\sim$12 bright stars in each pointing to models created by ray tracing through the optical design (Krist 2003). This achieves a repeatable precision of 1 μm in the determination of the focal length, and we construct a PSF model from all those stars observed during the 600-orbit COSMOS survey at a similar focus (Rhodes et al. 2007). We finally use this PSF model to correct the shapes of galaxies, and to obtain estimates of the amount by which their light has been sheared. The result is a catalogue of 1205 galaxies with shear estimates, corresponding to a density of $\sim$62 galaxies arcmin^{-2}.

2.3.2 VLT/FORS1

The complementary VLT data for our weak-lensing analysis are identical to that included by Cypriano et al. (2004) in a study of 24 X-ray Abell clusters. The total field of view is 6.8 arcmin on a side, centred on the cluster BCG and significantly exceeding the coverage of our *HST* imaging. *V*-, *R*- and *I*-band imaging was obtained with the FORS1 camera between 2001 April and July, with exposure times of 330 s in each filter. The data were reduced with standard IRAF routines and, to maximize the depth, we perform weak-lensing shape analysis on the combined *VRI* image. Seeing conditions were excellent, with a full width at half-maximum (FWHM) of stars in the combined *VRI* image of 0.59 arcsec.

We measure galaxy shapes and perform PSF correction using the `IM2SHAPE` method (Bridle et al. 2002). This involves a two-step process to first map the PSF variation across the observed field using stars, then to model each detected galaxy, perform PSF correction and recover its ellipticity. To remove foreground contamination and unreliable shape measurements from our catalogue, we apply magnitude cuts plus additional rejection criteria (see Cypriano et al. 2004). Since that work, we have improved the efficiency of foreground galaxy removal and now keep a higher density of background galaxies in our shear catalogue. The result is a catalogue of 912 galaxies with shear estimates, or $\sim$20 galaxies arcmin^{-2}.

2.3.3 Subaru/SuprimeCam

To extend the total field of view even further, especially in the Northern areas of the cluster field, we obtained 1.68 ks i'-band imaging data with Subaru/SuprimeCam during Semester S08B. The data were reduced following Okabe & Umetsu (2008), Okabe, Okura & Futamase (2010b) and Okabe et al. (2010a). Astrometric calibration was conducted by fitting the final stacked image with the Two-Micron All Sky Survey data point source catalogue; residual astrometric errors were less than the CCD pixel size. Due to poor weather conditions, the seeing size is as large as 1.28 arcsec.

We measure galaxy shapes and perform PSF correction using the IMCAT package (provided by Kaiser, Squires & Broadhurst 1995) in the same pipeline as Okabe et al. (2010a,b) with some modifications following Erben et al. (2001). Background galaxies were selected in the range of $22 < i' < 26$ABmag and $\bar{r}_{\rm h}^* + \sigma_{r_{\rm h}^*} \simeq 3.4 < r_{\rm h} < 6.0$ pixel, where $r_{\rm h}$ is the half-light radius, and $\bar{r}_{\rm h}^*$ and $\sigma_{r_{\rm h}^*}$ are the median and standard error of stellar half-light radii $r_{\rm h^*}$, corresponding to the half median width of the circularized PSF. The density of background galaxies in our final shear catalogue is $\sim$15 galaxies arcmin^{-2}. This is 30–50 per cent of typical values from images obtained during normal weather conditions (Okabe et al. 2010a,b).

2.4 Combined lensing reconstruction

In order to combine the weak- and strong-lensing constraints in a consistent way, we use the joint lensing reconstruction algorithm described in Merten et al. (2009) (see also Bradač et al. 2005, 2009, for a similar approach). This method has been extensively tested in Meneghetti et al. (2010a) and proved its capability to faithfully recover the cluster mass distribution over a broad range of scales.

Our joint mass reconstruction is non-parametric, in the sense that it neither makes any a priori assumptions about the cluster's underlying mass distribution nor does it need to trace any light-emitting component in the observed field. However, as described in Section 2.2, we use a parametric method to identify the multiple-image systems in the field. We reconstruct the cluster's lensing potential (its gravitational potential projected on to the plane of the sky) ψ by combining measurements of the position of the critical line and the reduced shear. To do this, we divide the observed field into an adaptive mesh, which discretizes all observed and reconstructed quantities. A statistical approach is chosen to combine our various measurements by defining a multicomponent χ^2-function that depends on the underlying lensing potential and a regularization term $R(\psi)$ to prevent the reconstruction overfitting noise (see Bradač et al. 2005; Merten et al. 2009)

$$\chi^2(\psi) = \chi^2_{\rm w}(\psi) + \chi^2_{\rm s}(\psi) + R(\psi). \tag{5}$$

The weak-lensing term is defined by the expectation value of the complex reduced shear in each mesh position $\langle\varepsilon\rangle$, which is obtained by averaging the measured ellipticities of all background galaxies within that grid cell

$$\chi^2_{\rm w}(\psi) = \left(\langle\epsilon\rangle - \frac{Z(z)\gamma(\psi)}{1 - Z(z)\kappa(\psi)}\right)_i \mathcal{C}^{-1}_{ij} \left(\langle\epsilon\rangle - \frac{Z(z)\gamma(\psi)}{1 - Z(z)\kappa(\psi)}\right)_j , \tag{6}$$

where $Z(z)$ is a cosmological weight factor as defined e.g. in Bartelmann & Schneider (2001), and $\gamma = \partial\partial\psi/2$ is the shear of the lens, with the two components expressed in complex notation. $\kappa = \partial\partial^*\psi$ is the convergence, where the complex differential operator in the plane is defined as $\partial := (\frac{\partial}{\partial\theta_1} + \mathbf{i}\frac{\partial}{\partial\theta_2})$, with θ_1 and θ_2 being the two angular coordinates in the sky. The indices i, j indicate the discretization of the input data and the lens properties, where we have to take into account the full χ^2-function because the averaging process of background galaxies might result in an overlap of neighbouring mesh points, expressed by the covariance matrix $\mathcal{C}_{ij}$.

The strong-lensing term is defined as

$$\chi^2_{\rm s}(\psi) = \frac{(\det \mathcal{A}(\psi))^2_k}{\sigma^2_{\rm s}} = \frac{\left((1 - Z(z)\kappa(\psi))^2 - |Z(z)\gamma(\psi)|^2\right)^2_k}{\sigma^2_{\rm s}} , \tag{7}$$

where the index k labels all pixels in the reconstruction mesh, which are supposed to be part of the critical curve within the uncertainties $\sigma_{\rm s}$, given by the pixel size of the grid. At these points, the Jacobian determinant $\det \mathcal{A}(\psi)$ of the lens mapping must vanish.

We iterate towards a best-fitting lens potential by minimizing the χ^2-function at each mesh position

$$\frac{\partial\chi^2(\psi)}{\partial\psi_l} \stackrel{!}{=} 0 \quad \text{with} \quad l \in [0, \ldots, N_{\rm pixel}] . \tag{8}$$

In practice, we achieve this by translating this operation into a linear system of equations and invoking a two-level iteration scheme (see Merten et al. 2009, and references therein).

In this analysis, we use all strongly lensed multiple-image systems from the confident sample (Table 1) together with their derived redshifts, and combine weak-lensing shear catalogues from all three telescopes (see Section 2.3) as described in Section 2.4.1. The combination of strong-lensing data and the density of background galaxies allows for a reconstruction on a mesh of 72×72 pixels in the central region (corresponding to a pixel-scale of 8.4 arcsec pixel^{-1}) and 36×36 pixels in the outskirts of the field (corresponding to a pixel-scale of 16.7 arcsec pixel^{-1}). Error estimates were produced by bootstrapping the redshift uncertainties of the strong-lensing constraints, and resampling those multiple-image systems in Table 1, which are marked with an asterisk. The result are 500 different bootstrap realizations of the refined cluster core. 150 bootstrap realizations of the cluster outskirts were produced by bootstrapping the combined ellipticity catalogues. The number of bootstrap realizations is mainly constrained by runtime considerations. All error estimates are calculated from the scatter within the full bootstrap sample. If not stated differently, the given value reflects 68 per cent confidence level.

2.4.1 Combining the catalogues

In order to combine the three different catalogues of ellipticity measurements we used the following strategy. Clearly, the Subaru catalogue delivered the largest field of view but it was derived from only single-band imaging and under bad seeing conditions. Therefore, we decided to limit its field size to a box of 600×600 arcsec^2 around the centre of the cluster and to cut out the central $\sim 400 \times 400$ arcsec^2 part, which was sufficiently covered by *HST*/ACS and VLT exposures with better data quality. As a result, Subaru data only cover the outermost 200 arcsec on each side of the field.

One might argue that the combination of *HST*/ACS and VLT ellipticities in the innermost centre of the cluster is problematic, but indeed the galaxy density is three times higher in the *HST*/ACS field and clearly dominating the adaptive-averaging process of the non-parametric reconstruction algorithm that we used for the further analysis (compare Section 2.4 and Merten et al. 2009).

Another issue is the possible double-counting of galaxies, so we cross-correlated both catalogues with a correlation radius of 2.5 arcsec and found 160 double-count candidates over the full *HST*/ACS field. Given the pixel size of the final reconstruction, this translates to an insignificant average double-count probability of less than one galaxy per pixel. Furthermore, the weighting scheme of the adaptive-averaging process was implemented such that the highest weight of the VLT ellipticities was identical to the smallest weight of the *HST*/ACS ellipticities. Finally, the errors in the ellipticity measurement are treated in the joint reconstruction method in a purely statistical way by deriving the variance of the weight-averaged sample of ellipticities in each reconstruction pixel.

Table 1. The multiple-image system of Abell 2744.

Image-ID (⟨source⟩.⟨image⟩⟨additional knot⟩)	x (arcsec)	y (arcsec)	z
1.1	−35.10	−13.55	2.0 ± 0.3
1.2	−30.15	−23.95	
1.3	0.10	−35.40	
1.11	−33.60	−16.50	
1.21	−31.50	−21.55	
1.31	1.60	−35.85	
2.1	9.30	−11.50	2.0 ± 0.3
2.2	−34.25	12.35	
2.3	2.80	1.05	
(2.4)	−0.50	−7.10	
2.11	11.55	−7.65	
2.21	−32.55	13.90	
2.31	5.55	3.10	
(2.41)	−0.05	−4.15	
3.1	−10.10	22.65	4.0 ± 0.3
3.2	−7.40	22.95	
(3.3)	27.15	2.20	
4.1	−18.25	−9.00	3.5 ± 0.3
4.2	−29.25	−5.30	
4.3	18.05	−31.60	
5.1*	8.85	29.00	4.0 ± 0.5
5.2*	3.85	31.60	
5.3*	19.65	19.30	
6.1*	−38.15	−5.95	3.0 ± 0.5
6.2*	−24.25	−28.30	
6.3*	−0.60	−33.15	
7.1*	−37.35	−7.85	3.7 ± 0.5
7.2*	−27.85	−26.10	
7.3*	5.10	−34.85	
8.1	−10.70	20.90	4.0 ± 0.2
8.2	−8.00	21.40	
(8.3)	16.10	5.90	
9.1*	−6.65	−18.45	3.0 ± 0.5
9.2*	−2.80	−21.90	
(9.3)	−43.20	10.80	
10.1*	−6.65	−20.65	3.0 ± 0.5
10.2*	−3.55	−22.75	
10.3*	−44.90	11.00	
(11.1)	−16.00	−13.30	3.0 ± 0.5
(11.2)	−34.20	−4.65	
(11.3)	10.70	−31.55	

Note. If the image ID is shown in brackets, the image is not confidently reproduced by the lensing model described in Section 2.2. The systems marked with an asterisk were nicely reproduced by the parametric lensing model but we allow them to be resampled by our non-parametric reconstruction technique to allow for uncertainties in the number of identified strong-lensing features. All other images define a 'confident catalogue' of multiple-image systems and are used in our subsequent analysis. The x- and y-coordinates are relative to the brightest cluster galaxy (BCG) position ($\alpha_{J2000} = 3^{\circ}.58611$, $\delta_{J2000} = -30^{\circ}.40024$) in arcsec. Redshifts of each system and their respective error are derived from the model predictions.

To derive a physical surface mass density from the scaled lensing convergence one needs to know at least the mean redshift of the background galaxy population that was used to produce the ellipticity catalogues. Problems with the different depths of the fields and therefore with the final mass analysis should not be a crucial

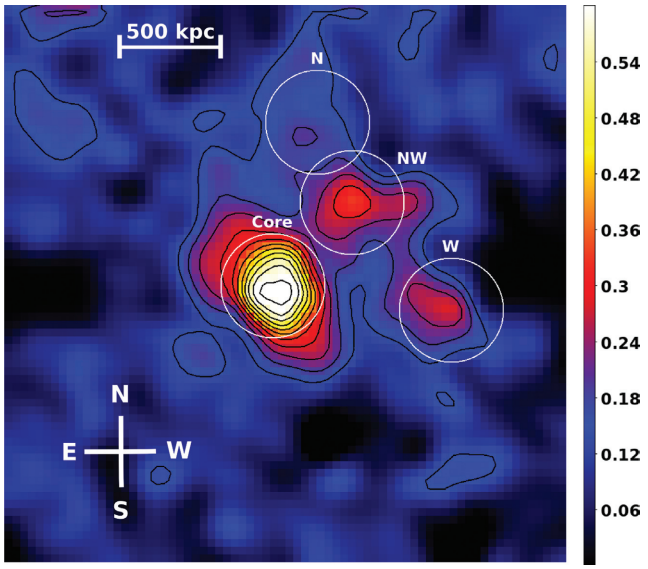

Figure 3. The convergence map of the cluster field for a source redshift of $z_s = \infty$ and a field size of 600 × 600 arcsec^2, translating to ∼2.7 Mpc on a side. The black contours start at $\kappa_0 = 0.14$ with a linear spacing of $\Delta\kappa = 0.047$. The four white circles with labels indicate identified subclumps and the radius within which their mass is calculated. The radius of all four circles is 55.4 arcsec ≈ 250 kpc.

issue for a relatively low redshift cluster like Abell 2744. However, the redshift for determining the surface mass density from the reconstructed convergence in the overlap area has been calculated as the galaxy-density weighted average of both the VLT and the *HST*/ACS populations. The redshifts of the strong-lensing features (compare Table 1) were included for the determination of the core mass, and the respective redshifts of the VLT and Subaru source distribution were used in the outskirts of the field.

In order to test the effect of dilution in the outskirts of the field, we increased the ellipticity values for all Subaru background galaxies by 15 per cent and repeated the reconstruction. This test is necessary due to the single-band Subaru imaging. As it turns out, the difference in the reconstructed convergence is marginal since the ellipticity values are already low with large scatter in this area of the field. However, the effect was included in the determination of the error budget for the reconstructed total mass and mass profile.

2.5 Reconstruction results

We obtain a map of the lensing convergence across the field (proportional to the projected mass) by applying the Laplacian operator to the lensing potential on the adaptively refined mesh (see Fig. 3). We find a total mass (by assuming $h = 0.7$ here and further on) within a radius of 1.3 Mpc around the Core of $M(r < 1.3\,\mathrm{Mpc}) = 1.8 \pm 0.4 \times 10^{15}\,\mathrm{M}_{\odot}$, which is in good agreement with kinematically derived masses (Boschin et al. 2006). A mass determination within a field of (1300 × 750) kpc [to compare easily to the work on the Bullet Cluster of Bradač et al. (2006)] centred on the Core density peak yields $M(1.73\,\mathrm{Mpc}^2) = 7.4 \pm 1.0 \times 10^{14}\,\mathrm{M}_{\odot}$, rendering Abell 2744 comparable in mass or slightly less massive than the Bullet Cluster (Bradač et al. 2006). The overall radial convergence and mass profile can be found in Fig. 4.

Most interestingly, our gravitational lensing analysis resolves four distinct sub-structures, indicated in Fig. 3 by the white circles. We label these substructures as Core, Northwestern (NW, later on

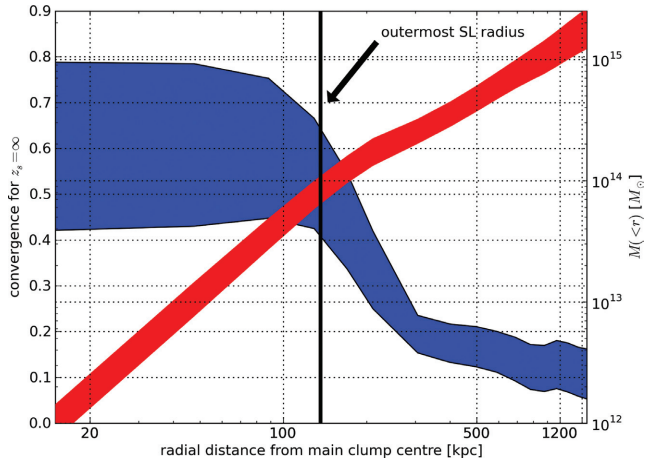

Figure 4. Radial mass profiles of the cluster, derived from our lensing analysis. Shown in blue (referring to the left y-axis) is the convergence profile for a source redshift $z_s = \infty$. The large uncertainty for small radii arises from uncertainty in the exact position of the cluster centre. The cumulative mass as a function of radial distance from the cluster centre is shown in red (referring to the right y-axis). The black vertical line indicates the distance of the outermost multiple images from the cluster centre.

Table 2. Structures identified within our lensing reconstruction.

Name	x (arcsec)	y (arcsec)	$M(r < 250\,\mathrm{kpc})$ ($10^{14}\,\mathrm{M}_\odot$)
Core	-13^{+11}_{-8}	-4^{+6}_{-13}	2.24 ± 0.55
NW	71^{+11}_{-10}	84^{+15}_{-7}	1.15 ± 0.23
W	177^{+23}_{-17}	-30^{+11}_{-15}	1.11 ± 0.28
N	34^{+23}_{-32}	170^{+10}_{-28}	0.86 ± 0.22

Notes. The x- and y-coordinates are provided in arcsec, relative to the BCG position ($\alpha_{J2000} = 3^\circ.58611$, $\delta_{J2000} = -30^\circ.40024$). The 68 per cent confidence limits on peak positions are derived from 500 bootstrap realizations for the Core peak, and from the pixel size of the coarse weak-lensing mesh in the reconstruction outskirts for the other mass peaks. Masses assume $h = 0.7$ and their 68 per cent confidence limits are derived from bootstrap realizations as described in the text.

dubbed as 'dark'), Western (W, later on dubbed as 'stripped') and Northern (N) structure. Please note that there is some indication of a possible double peak in the NW structure, as can be seen in Fig. 1 and also in the clearly visible extension of the structure towards the West in Fig. 3. The Core, NW and W clumps are clear detections in the surface mass density distribution with 11σ, 4.9σ and 3.8σ significance over the background level, respectively.[2] Somewhat fainter with 2.3σ significance is the N structure, but it clearly coincides with a prominent X-ray substructure found by Owers et al. (2011) and is therefore included in the further analysis (compare Section 3). The positions of the mass peaks and their local projected masses within 250 kpc are listed in Table 2 and shown in more detail in Fig. 1. The new *HST*/ACS images thus allow a striking improvement in our map of the mass distribution and reveal the distribution of dark matter sub-structure in great detail for the first time. We will refer to the individual mass clumps resolved here in our discussion of the X-ray analysis below.

[2] The background level was estimated in the following way: from the total convergence, shown in Fig. 3, a radial area of 75 arcsec around the Core, 70 arcsec around NW and 55 arcsec around N and W was cut out. From the remaining field the mean and variance in the convergence level were calculated.

3 X-RAY ANALYSIS

The most difficult part of interpreting merging clusters is determining the geometric configuration of the collision, such as its impact velocity, impact parameter and angle with respect to the plane of the sky (Markevitch et al. 2002). For this purpose, X-ray data become a crucial addition to lensing measurements. The location of any shock front is revealed in the temperature of the intracluster medium (ICM). Velocities can be inferred from the density and temperature of intracluster gas (if the merger axis is near the plane of the sky), or through direct Doppler measurements (if the merger axis is near the line of sight).

3.1 Reduction of the *Chandra* data

We reanalysed all existing *Chandra* data of Abell 2744 (listed in Owers et al. 2011), using CIAO 4.3 with the calibration data base CALDB 4.4.2. We cleaned the data using the standard procedure[3] and kept events with grades 0, 2, 3, 4 and 6. We removed the ACIS particle background as prescribed for 'VFAINT' mode, and applied gain map correction, together with Pulse Height Amplitude (PHA) and pixel randomization. Point sources were identified and removed, and the sky background to be subtracted from spectral fits was generated from Blank-Sky observations using the `acis_bkgrnd_lookup` script. We fit spectra using XSPEC V12.6.0Q (Arnaud 1996) and we adopt VAPEC thermal emission model from atomic data in the companion Astrophysical Plasma Emission Data base (Smith et al. 2001), allowing for the variation of several individual elemental abundances during the spectral fittings. Galactic photoelectric absorption is incorporated using the `wabs` model (Morrison & McCammon 1983). Spectral channels are grouped to have at least 20 counts per channel. Energy ranges are restricted to 0.5–9.5 keV. Metal abundances are quoted relative to the solar photospheric values of Anders & Grevesse (1989), and the spectral fitting parameter errors are 1σ unless stated otherwise.

There is a known reduction of quantum efficiency at energies below 1 keV due to a build-up of molecular contaminants on the optical blocking filter (or on the CCD chips).[4] To prevent this from affecting our measurement of low-energy line abundances, hydrogen column density and overall gas temperature, we fix the column density to the cluster's nominal value of $1.6 \times 10^{20}\,\mathrm{cm}^{-2}$ (Dickey & Lockman 1990). To be conservative, we present results from only those regions of the CCDs which are best-suited for velocity analysis (ACIS-I pointings 8477 and 8557); for an independent sanity check, we also repeat the analysis with ACIS-S pointing 2212. We exclude pointings 7712 and 7915 because the regions of interest cross multiple CCDs, and interchip gain fluctuations could introduce spurious systematic effects when measuring the redshifts from X-ray spectra.

Since spectral models are (weakly) degenerate with cluster redshift, it is common for simultaneous fitting routines to get stuck in local χ^2 minima before they reach the global best fit. We circumvent this via an iterative approach. We perform initial fits while

[3] http://cxc.harvard.edu/ciao/guides/acis_data.html
[4] http://cxc.harvard.edu/cal/Links/Acis/acis/Cal_prods/qeDeg/index.html

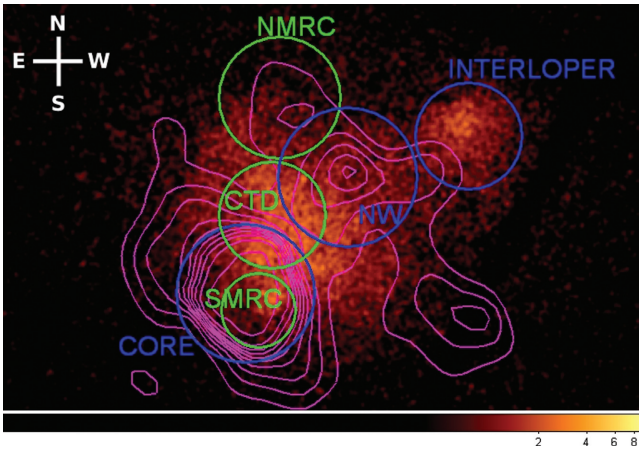

Figure 5. X-ray image of Abell 2744, overlaid with our lensing mass reconstruction (magenta). The velocity gradient is maximal between three regions of interest named by Owers et al. (2011) and circled in green (SMRC, NMRC and CTD). A velocity gradient is also detected between the regions of interest from our lensing mass reconstruction, circled in blue (Core and NW) as well as the interloper.

varying the redshift values within reasonable ranges (via the command STEPPAR in XSPEC). We then fix the redshift, and refit full spectral models to infer gas temperature, metal abundances and normalizations. Subsequently, we use these best-fitting values as inputs in a new fit with the redshift free to vary. This provides a more reliable estimation of the error on the redshift measurement. We repeat the process until the best-fitting redshift no longer changes between iterations.

3.2 Previous X-ray observations and interpretations

Abell 2744 shows an extremely disturbed X-ray morphology (compare Fig. 5). With 25 ks of *Chandra* ACIS-S3 imaging, Kempner & David (2004) decided it is the aftermath of a N–S collision between similar-mass proto-clusters, at Mach >2.6. They also found tentative evidence for a cold front in the detached nearby NW 'interloper', which they guessed was falling into the main cluster. Owers et al. (2011) obtained a further 101 ks of ACIS-I imaging. The deeper data revealed the 'Southern minor remnant core' (SMRC) to be colder ($T_X \sim 7.5$ keV) than its surroundings, with a high-temperature region to the SE ($T_X > 15$ keV) that they interpreted as a shock front. They concluded the SMRC had been a low-mass bullet that has passed through the 'Northern major remnant core' (NMRC), leaving central tidal debris (CTD). The pressure ratio of ∼3:1 across the shock front corresponds to a sky-projected shock velocity of 2150 km s^{-1} (for an average temperature $T_X \sim$ 8.6 keV). Owers et al. (2011) reversed the Kempner & David (2004) model of the interloper, concluding that it came originally from the South, has already passed through the main body of the host cluster with a large impact parameter and is now climbing out towards the N-NW.

Owers et al. (2011) also obtained spectra of more than 1200 galaxies with the Anglo-Australian Telescope multifibre AAOmega spectrograph, and confirmed the velocity bi-modality of the cluster galaxies. One component of galaxies near the SMRC has a peculiar velocity of 2300 km s^{-1}; a separate component near the NMRC has a peculiar velocity of about −1600 km s^{-1} and enhanced metal abundances (∼0.5 solar). Assuming that the Northern and Southern cores have the same velocities as the 'apparently' associated galaxy populations, they de-projected the velocity of this collision to Mach 3.31 or nearly 5000 km s^{-1}.

An interesting prediction of this scenario is that the intracluster gas should show a strong radial velocity gradient of ∼4000 km s^{-1} or $\Delta z \sim 0.014$ from North to South. Since the intracluster medium is enriched with heavy elements, radial velocity measurements could be carried out directly by measuring the Doppler shift of emission lines in the X-ray spectrum (Dupke & Bregman 2001a,b; Andersson & Madejski 2004; Dupke et al. 2007) or through changes in line broadening due to turbulence (Inogamov & Sunyaev 2003; Sunyaev, Norman & Bryan 2003; Pawl, Evrard & Dupke 2005). The former requires high photon counts within the spectral lines and excellent control of instrumental gain but could, in principle, be measured with current X-ray spectrometers. The latter requires very high spectral resolution that should become available through the future *ASTRO-H* and *IXO* satellites (however, see Sanders et al. 2010; Sanders, Fabian & Smith 2011).

The existing data are not ideal for measurements of ICM velocity structure with high precision due to the variation of gain expected from the analysis of multiple observations with different pointings and in different epochs. However, the expected radial velocity gradient of 4000 km s^{-1}, predicted from the optical work of Owers et al. (2011), is higher than the expected interchip and intrachip gain variations, so that it becomes possible to test, even if just for consistency, the proposed merger configuration, as we did in this work. *Chandra* has a good gain temporal stability (Grant 2001) and we shall control for spatial variations by performing resolved spectroscopy of multiple cluster regions using *the same CCD location* in different ACIS-I pointings.

3.3 Velocity measurements

We perform our velocity analysis twice: for the regions of interest defined by Owers et al. (2011), and then for the substructures prominent in our lensing mass maps. These are respectively indicated by green or blue circles in Fig. 5.

We find temperature and metal abundance values for the NMRC, CTD and SMRC regions of 8.29 ± 0.67 keV and 0.55 ± 0.18 solar ($\chi_\nu = 1.06$ for 234 degrees of freedom); 9.51 ± 0.47 keV and 0.27 ± 0.08 solar ($\chi_\nu = 1.03$ for 469 degrees of freedom); and 7.98 ± 0.76 keV and 1.17 ± 0.51 solar ($\chi_\nu = 1.01$ for 143 degrees of freedom). These values are derived from simultaneous fits to pointings 8477, 8557 and 2212. The values are consistent with those obtained through individual spectral fits for each instrument/observation (two independent ACIS-I and one ACIS-S). Our temperature and abundance measurements are thus consistent with the values found by Owers et al. (2011). Given that the observations were not tailored for velocity measurements (i.e. we cannot exclude temporal or inter-chip gain variations), we conservatively include in our velocity error bars secondary χ^2 minima that are separated from the global minimum at less than 90 per cent confidence in the velocity measurements.

Our velocity measurements are consistent with the presence of a gradient between the NMRC and SMRC, but in the opposite sense to that expected from Owers et al. (2011) interpretation. Using the ACIS-S, the CCD with the best spectral response, the velocity difference between NMRC and SMRC is found to be >1500 km s^{-1} at 90 per cent confidence.

The observations (8477 and 8557) indicate a higher magnitude for the velocity gradient detected. However, the central values of the

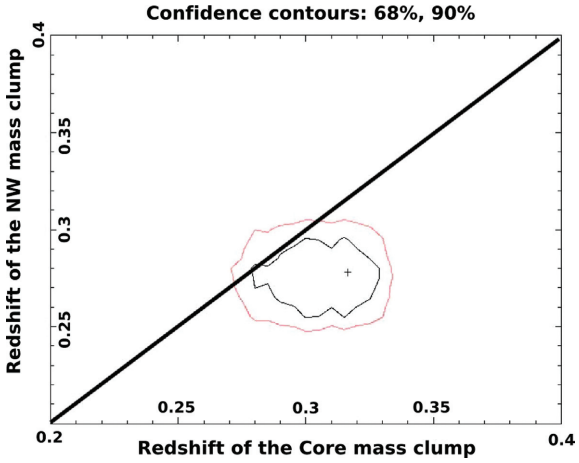

Figure 6. Simultaneous fits to the redshifts of the Core region and the NW substructure using two ACIS-I and one ACIS-S pointings. The two contours correspond to 68 per cent (inner) and 90 per cent (outer) confidence levels, and the diagonal line indicates equal redshifts to guide the eye. The Core mass clump appears significantly redshifted when compared to the NW mass clump.

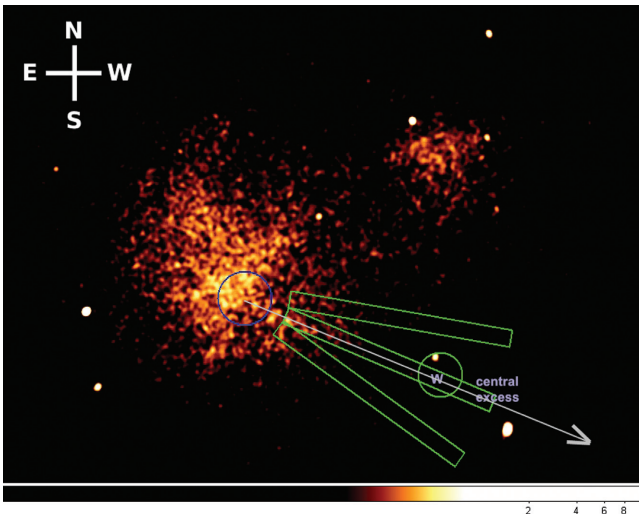

Figure 7. *Chandra* ACIS-S3 X-ray image of Abell 2744, smoothed with a 3 pixel kernel Gaussian. We analyse the cluster's X-ray profile in three rectangular regions, each 150 arcsec in length and radiating from the cluster centre (marked by the blue circle). We find marginally significant excess X-ray emission in the central rectangular region, which extends towards the Western clump (marked by the green circle).

best-fitting redshifts in each observation are found to be significantly discrepant, introducing larger uncertainties. The reason for this discrepancy is not clear, but it is possibly related to the observed focal plane temperature variation of about 0.9 °C between these observations (Catherine Grant, personal communication). This explanation is supported by the marginally significant observed systematic difference of ∼10–20 per cent in the best-fitting values of temperatures and abundances measured for the same regions in these different ACIS-I observations. This effect was also noted in Owers et al. (2011) (M. Owers, personal communication). Therefore, although our analysis is consistent with a high-velocity gradient, the direction of the gradient does not corroborate the merger configuration suggested by Owers et al. (2011).

Having the lensing mass reconstruction shown in the previous sections at hand we can study the line-of-sight gas velocity mapping for the regions of interest (Core and NW) more precisely. Using all three exposures, we measure their gas temperatures and metal abundances to be $T_{\mathrm{X_{Core}}} = 10.50 \pm 0.57$ keV, $\mathrm{A_{Core}} = 0.28 \pm 0.11$ solar with a reduced chi-squared $\chi_\nu = 0.90$ for 466 degrees of freedom and $T_{\mathrm{X_{NW}}} = 10.22 \pm 0.54$ keV, $A_{\mathrm{NW}} = 0.40 \pm 0.09$ solar with $\chi_\nu = 0.91$ for 477 degrees of freedom.

Despite their similar gas properties, these regions show a velocity gradient >5200 km s^{-1} at near 90 per cent confidence, even including a conservative (1σ) intra-chip gain variation of 1000 km s^{-1} (e.g. Dupke & Bregman 2006) per CCD in the error budget, in quadrature. A contour plot of the velocity difference is shown in Fig. 6. This result is consistent with the idea that the Southern Core mass is *redshifted* with respect to other structures. None the less, these calculations should be taken with caution due to the uncertainties related to temporal gain variations and inter-chip gain variations between ACIS-I and ACIS-S. The same analysis using only the ACIS-I observations shows the same velocity trend, but with a reduction in the absolute velocity difference (an upper limit of <4400 km s^{-1} at the 90 per cent confidence level). Deeper *Chandra* observations, specifically tailored for velocity measurements, will be crucial to further reduce uncertainties and to better constrain the velocity structure of this cluster.

4 INTERPRETING THE MERGER

Abell 2744 is undoubtedly undergoing a complicated merging process on a large cluster scale. Progressively more detailed studies, culminating in our lensing reconstruction (Section 2) and X-ray analysis (Section 3), have only agreed that the merger is more complex than previously thought. For example, the likely explanation for the gas velocity gradient in the opposite direction to that expected by Owers et al. (2011) is that the NMRC is *not* the main cluster. Our lensing mass reconstruction shows that the deepest gravitational potential is by far the Southern 'Core' structure, which is roughly coincident with Owers et al.'s SMRC but slightly further offset from the Compact Core. We also find three separate mass concentrations to the North, Northwest and West. Overlaying the lensing mass reconstruction and X-ray emission in Fig. 1 reveals a complex picture of separations between the dark matter and baryonic components. To interpret the sequence of events that led up to this present state, we shall now tour the regions of interest, with more detailed discussions.

4.1 Core, the massive clump

According to our lensing analysis, the Core region (lower-left quadrant of Fig. 1) is by far the most massive structure within the merging system (cf. Table 2). All the strong-lensing features can be seen within this clump. We find no large separation between the distribution of mass and baryonic components. The mass peak is centred amongst the bright cluster member galaxies (within 1σ errors, it is consistent with the position of the BCG) and only 22 ± 12 arcsec from a peak of X-ray emission identified by Owers et al. (2011). We support the general conclusion of Owers et al. (2011) that the major merger in Abell 2744 is similar to that of the Bullet Cluster as it would be seen at a large inclination with respect to the plane of the sky. However, we reverse the ordering of the major and minor mass components.

One can infer constraints on the collisional cross-section of dark matter from the separation between peaks in the lensing and

X-ray maps. For the Bullet Cluster, Markevitch et al. (2004) found $\sigma/m < 5\,\mathrm{cm^2\,g^{-1}}$, and for the Baby Bullet, Bradač et al. (2008) found $\sigma/m < 4\,\mathrm{cm^2\,g^{-1}}$. In the Core of Abell 2744, we observe a projected 17 arcsec separation that, if the inclination is $\sim 30^\circ$ away from the line of sight (Owers et al. 2011), is a physical separation similar to that in the other bullet clusters. For an order of magnitude analysis, we measure the mean surface mass density within 150 kpc of the mass peak $\Sigma \simeq 0.30^{+0.08}_{-0.07}\,\mathrm{g\,cm^{-2}}$, so that the scattering depth $\tau_\mathrm{s} = \sigma/m\,\Sigma$. With the assumption $\tau_\mathrm{s} < 1$, which is justified due to the observed dark matter–gas separation, we deduce $\sigma/m < 3 \pm 1\,\mathrm{cm^2\,g^{-1}}$. This system may therefore yield one of the tightest constraints on the interaction cross-section of dark matter, based on such analysis. A full numerical simulation to interpret the cluster configuration would be ideal, especially given the uncertainty in the collision angle with respect to the plane of the sky. Indeed, even tighter constraints ($\sigma/m < 0.7\,\mathrm{cm^2\,g^{-1}}$) were obtained from the Bullet Cluster by Randall et al. (2008), who interpreted the offsets between all three cluster components via tailored hydrodynamical simulations. Additional constraints on the collisional cross-section have also recently been obtained from dark matter stripping in Abell 3827 (Carrasco et al. 2010; Williams & Saha 2011) and the ellipticities of dark matter haloes (Miralda-Escudé 2002), with implications discussed in Feng, Kaplinghat & Yu (2010).

4.2 Northern, the bullet

Our analysis of the Northern mass substructure (upper-left quadrant of Fig. 1) confirms the overall North–South merging scenario proposed by several authors in the past. We find a mass ratio of ∼2.6 between the Core and the Northern clump, roughly supporting the 3:1 merging scenario of Boschin et al. (2006), but we identify the Northern sub-clump as the less massive progenitor. This conclusion is robust, with no strong-lensing features revealed by even our high-resolution *HST* imaging in the Northern structure, as would have been expected for the reversed mass ordering proposed by Owers et al. (2011).

X-ray emission in the Northern mass substructure lags behind the dark matter as expected. We measure a separation of ∼30 arcsec to the South. This is a similar separation to that in the core but, due to the lower surface mass density in this region, constraints on the collisional cross-section are less significant.

4.3 Northwestern, the ghostly and dark clumps

By far, the most interesting structure is located to the Northwest of the cluster field (upper-right quadrant of Fig. 1). Our lensing analysis (Section 2.5) shows it to be the second-most massive structure. A separate region of X-ray emission also lies to the Northwest, called the NW interloper by Owers et al. (2011). Furthermore, in 54 per cent of our weak-lensing bootstrap realization we identified a second peak in the more Western area of the NW mass clump (see Fig. 1), rendering it difficult to say if we indeed see a single, separate dark matter structure and to derive decisive separation between dark matter, X-ray luminous gas and bright cluster member galaxies. However, the separation between our different possible NW mass peak positions and the NW interloper is large (>150 kpc for NW2). When compared to the more prominent Eastern mass peak NW1, which is identified in 95 per cent of the bootstrap realizations, the distance is even at least 400 kpc.

With a de-projected temperature of ∼5 keV (Owers et al. 2011) the NW interloper should have $r_{500} \sim 1.34$ Mpc (Evrard, Metzler & Navarro 1996) and $M_{500} \sim 4$–$5 \times 10^{14}\,\mathrm{M_\odot}$ (e.g. fig. 8 of

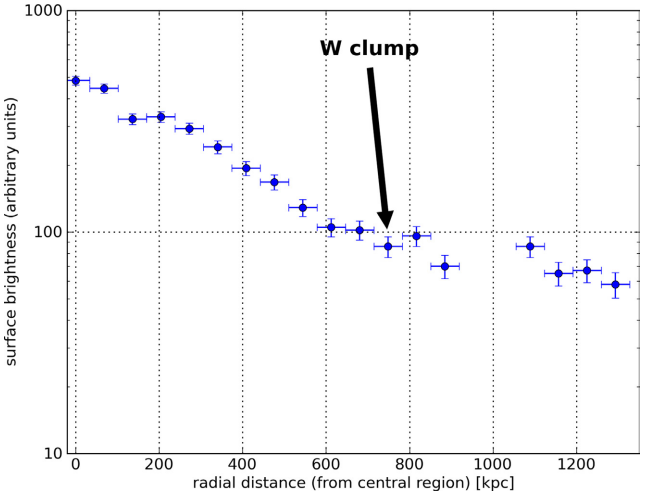

Figure 8. Surface brightness profile (in arbitrary units) of the central rectangular region shown in Fig. 7. The left-hand side starts at the X-ray centre, and the arrow denotes the approximate position of the Western mass clump. The abrupt change in profile slope at roughly the same location is highlighted by the intersection with the horizontal line.

Khosroshahi, Ponman & Jones 2007). Its 0.1–10.0 keV unabsorbed luminosity is $2.5 \times 10^{44}\,\mathrm{erg\,s^{-1}}$, consistent with its gas temperature of 4–5 keV (Khosroshahi et al. 2007; Díaz-Giménez et al. 2011). Assuming a β (from a King-like profile) of 0.67, typical for clusters, the clump would have $\sim 0.95 \times 10^{14}\,\mathrm{M_\odot}$ within 250 kpc, similar to the N clump, and should have been easily detected in the lensing analysis. The interloper thus appears to be an X-ray feature with no associated dark matter or galaxies, and we therefore dub it the 'ghost' cluster.

There is also a clear separation between the peak of the NW mass clump and any cluster member galaxies, so we call this the 'dark' cluster. Contours of the lensing mass reconstruction extend towards the West, where indeed we find a pair of giant ellipticals (see Fig. 1). However, with the limited resolution of the VLT weak-lensing reconstruction, it is impossible to tell whether this is a binary mass structure, though there are clear indications for that in our analysis of this mass clump.

The separation between all three mass components makes this a real puzzle and it should be stressed that such a peculiar configuration is observed for the first time. It may pose another serious challenge for cosmological models of structure formation. One possible explanation was suggested by Owers et al. (2011), who describe it as a ram-pressure slingshot (e.g. Markevitch & Vikhlinin 2007). In this interpretation, after first core-passage, gas initially trails its associated dark matter but, while the dark matter slows down, the gas slingshots past it due to a combination of low ram-pressure stripping and adiabatic expansion and cooling, which enhances the cold front temperature contrast (Bialek, Evrard & Mohr 2002). There is indeed a clear velocity gradient between the NW interloper and the main cluster core (see Section 3). Such effects have also been observed e.g. in Abell 168 (Hallman & Markevitch 2004), in a joint weak-lensing and X-ray study of Abell 754 (Okabe & Umetsu 2008) and in numerical simulations (Mathis et al. 2005; Ascasibar & Markevitch 2006), although at a much smaller separations between dark matter and gas. The more than 100 arcsec separation in Abell 2744 suggests either that the slingshot scenario is unlikely or that some amplifying mechanism is in place. We shall return to this issue, proposing an interpretation of the entire cluster merger, at the end of this section.

4.4 Western, the stripped clump

The Western substructure (lower-right quadrant of Fig. 1) has not yet been discussed in the literature, but several cluster member galaxies are found in this area. We find a prominent weak gravitational lensing signal of $\sim 1.0 \times 10^{14}\,M_{\odot}$ within 250 kpc. This should correspond to an X-ray brightness higher than the NW interloper, for the same gas temperature. However, we detect no X-ray emission. The best X-ray data (ACIS-I pointings 8477 and 8557) do not cover the region of this lensing signal, but the ACIS-S pointing 2212 indicates no excess diffuse gas above the cosmic background and the extended tail of the cluster's outskirts. To match these observations, the Western clump must have been completely stripped of its ICM, so we dub it the 'stripped' clump.

The only slight excess X-ray emission nearby is a faint extension of the main cluster core towards the West ('ridge c' in Owers et al. 2011). This roughly links the Western clump to the Northern clump, and is consistent with remnants stripped by ram pressure during a secondary merging event (NE–SW), almost perpendicular to the main merging event projected in the sky plane. To quantify the excess X-ray emission, we measure counts inside three equal-sized, non-overlapping regions extending from the cluster core to a radial distance of 150 arcsec $\approx$ 680 kpc, as shown in Fig. 7. To prepare the data for this analysis, we divide the image by the exposure map following the standard procedure, remove hot pixels and remove point sources using the `dmfilth` routine in CIAO. We find a marginal excess in the central box (1030 ± 32 counts), which points to the Western clump, above the Northern (965 ± 31 counts) and Southern (876 ± 29 counts) boxes. The cluster's surface brightness profile from the core towards the Western clump (along the central box) is shown in Fig. 8. The slope of the profile changes at a radius $\sim$135 arcsec = 612 kpc away from the centre, becoming significantly shallower. If we take that point of transition as the location of the remaining gas core, we obtain a separation between the gas and dark matter of 30 arcsec. Similar results are found with the shallower observation 7915 using ACIS-I.

We find a slight offset between the peak of the lensing mass reconstruction and the most luminous nearby cluster member galaxies. However, there is large uncertainty in the position of the lensing peak because this lies outside the *HST* imaging area. Our weak-lensing analysis uses only VLT imaging, and there are no strong-lensing constraints, so the mass reconstruction has a broad central plateau. Additional *HST* observations would provide an ideal foundation to better understand the Western area, which turns out to be playing a significant role in the overall merger.

4.5 One possible interpretation

We shall now try to develop a possible explanation of the complex merging scenario that has taken place in Abell 2744. To recap, we find four mass clumps (Core, N, NW, W) with approximate masses 2.2, 0.8, 1.1, 1.1 $\times 10^{14}\,M_{\odot}$, respectively. The Core, N and W clumps are relatively close to BCGs and hot gas. The NW structure, on the other hand, contains separated dark matter, gas and galaxies.

We propose that the current configuration is the result of a near simultaneous double merger, as illustrated in Fig. 9. The first merger, in the NE–SW direction, had a characteristic path of 208 arcsec (plane of the sky distance between N and W clumps) or $\sim$0.95 Mpc (assuming no line-of-sight velocity component). The Western clump probably passed closest through the main cluster, as it had its ICM ram pressure stripped completely. The second merger, in the SE–NW direction, had a characteristic path of 117 arcsec/sin (27°) $\approx$ 1.17 Mpc, if we assume the inclination of that merger suggested by Owers et al. (2011) of 27°. The mergers happened around 0.12–0.15 Gyr ago, with a characteristic velocity of $\sim$4000 km s^{-1} as indicated by the galaxy velocity difference and the ICM gas velocity measurements.

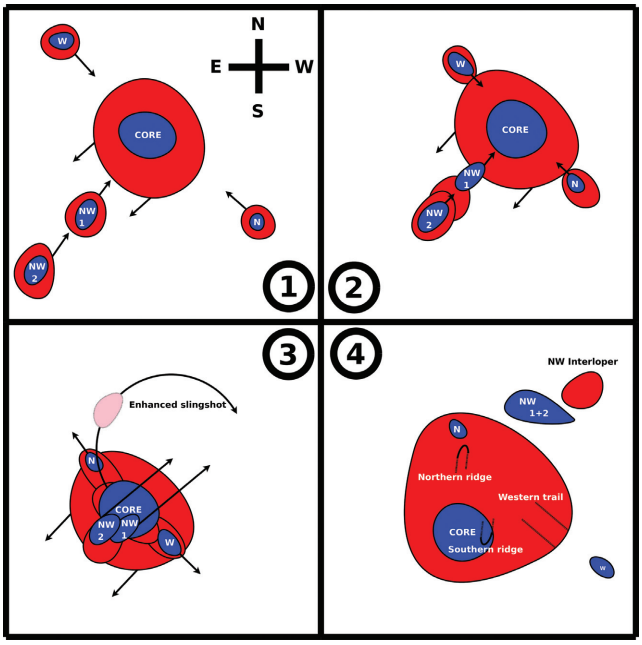

Figure 9. Our proposed merging scenario, illustrated in time-ordered sequence, to explain the current configuration (panel 4). We suggest that Abell 2744 is the result of a nearly simultaneous double merger: one in the NE–SW direction and another in the NW–SE direction, which may even have consisted of three separate structures falling along a filament. Blue colour indicates the innermost dark matter cores of the clumps, whereas their respective ICM is shown in red.[5]

It is possible that the merger in the SE–NW direction could even have consisted of three initial substructures: the Core and two consecutive clumps [with a combined mass (within 250 kpc of each core) of $\sim 1.2 \times 10^{14}\,M_{\odot}$] falling along a filament. Those smaller clumps would be accelerated by the gravitational pull of the main cluster (plus the Northern and Western clumps, which were merging perpendicularly). The ram-pressure slingshot in these clumps could be enhanced by a combination of an initially stronger gravitational field and perhaps a posterior reduction in ram pressure due to the 'puff-up' of the gas density due to the recent merger of Core+N+W, similar to the density configuration of the main component in the Bullet Cluster. The combined effect would throw the gas component ahead of its associated dark matter, forming the 'ghost' cluster, which is now the interloper. The two dark matter clumps left behind would now form the possibly double-centred 'dark' clump.

This unusual scenario fits the current observations. It explains the clear extension of the NW clump towards the West and provides probably a mechanism to create such a huge separation between dark matter and gas in the NW area. However, the double peak in the NW clump needs to be confirmed by an additional *HST* pointing to cover its full area. The discovery of a second distinct mass peak in the NW clump would support our merger scenario and also decrease the large measured separations between dark matter, gas and bright

[5] A video and animation illustrating our merger scenario can be accessed at http://www.spacetelescope.org/videos/heic1111a/ and http://www.spacetelescope.org/videos/heic1111b/.

cluster galaxies. Also the ghostly interloper has not been covered by the current *HST* observations and the Western clump falls between chip gaps in the longer *Chandra* exposures, so further observations will still be required. Our suggestions will also eventually require verification via a set of well-tailored numerical simulations and have to be taken with some caution at the current stage. Cosmological boxes have to be explored (compare Meneghetti et al. 2010b, 2011) in order to find similar configurations and detailed, hydrodynamical simulations need to repeat and confirm our findings.

5 CONCLUSIONS

We present a detailed strong-lensing, weak-lensing and X-ray analysis of the merging cluster of galaxies Abell 2744. Earlier studies (Kempner & David 2004; Boschin et al. 2006; Braglia et al. 2009; Owers et al. 2011) concluded that Abell 2744 is undergoing a complicated merging event. We find that it is even more complex than previously thought, unleashing a variety of exciting effects. We dub this merger therefore *Pandora's cluster*.

Deep, three-band *HST* imaging reveals a variety of strong-lensing features in the core of the cluster. From our comprehensive strong-lensing modelling of the central mass distribution, we identify a total number of not less than 34 multiple images, in 11 multiple-image systems, together with their respective redshifts. The strong-lens systems are listed in Table 1 and the finely resolved critical curve of the cluster core is shown in Fig. 2. The Einstein radius of the core is $r_{\rm E} = 30 \pm 3$ arcsec.

We extended the strong-lensing information with weak-lensing measurements over the whole cluster system (600×600 arcsec^2, or $\sim$2.7 Mpc on a side). The shapes of background galaxies necessary for weak-lensing reconstruction were obtained from a comprehensive combination of our new *HST*/ACS imaging, the VLT data used in Cypriano et al. (2004), and additional Subaru imaging. Our combined strong and weak-lensing mass reconstruction (Fig. 3) resolves a complex structure, with at least four distinct peaks in the local mass distribution. The total mass of the cluster is $1.8 \pm 0.4 \times 10^{15}\,{\rm M}_{\odot}$ within a radius of 1.3 Mpc, rendering Abell 2744 similar in mass to the Bullet Cluster.

Chandra X-ray imaging also shows a complex arrangement of substructure. There are at least four X-ray ridges departing from the X-ray peak, including a Northern (NMRC) and a Southern (SMRC) ridge (Owers et al. 2011). Interestingly, none of these coincides with any of the mass clumps found in our lensing mass reconstruction. Furthermore, the system also has a separate Northwestern X-ray feature with very low mass, also undetected in our lensing analysis. Observations of the gas temperature in this Northwestern feature (Kempner & David 2004; Owers et al. 2011) show a cold front pointing N-NE and a shock region ($T_{\rm X} > 15$ keV) in the Southern ridge, for a projected impact velocity of 2150 km s^{-1}. That projected direction (SE–NW) therefore seems to define the primary merging event. However, in contrast to the proposed merging scenario of Owers et al. (2011), we find the Southern ridge to be blueshifted with respect to the Northern ridge.

We also reveal that the Southern Core is $\sim$2.6 times more massive than the Northern sub-clump – Owers et al. (2011) had expected this reverse – and that the secondary mass peak is in the Northwest. The mass ratio thus remains in agreement with general kinematical studies of Boschin et al. (2006), but swaps the sense of the collision from Owers et al. (2011). With this new scenario in hand, we repeated the velocity gradient analysis using the 'true' mass clumps (Core and Northwestern). These regions exhibit similar gas temperatures and metal abundances, and show evidence for a >5200 km s^{-1} velocity gradient with the Core region redshifted. These limits should be taken with caution, since the *Chandra* observations were not tailored specifically for velocity studies (they were obtained in different CCDs and at different epochs, so could be affected by variations in detector gain), and there is also some evidence of unknown calibration uncertainty between the two ACIS-I pointings taken of the same patch of sky. However, our results are consistent with the main merger having a significant component along the line of sight, with a magnitude and orientation consistent with that seen in the bi-modal distribution of galaxy velocities.

We also find evidence for a second merging event, simultaneously with or just before the main merger. The second merger, along the perpendicular NE–SW axis, was between today's Northern and Western mass peaks. We think these collided inside the extended halo of the core. During this dramatic collision, gas in today's Northern 'bullet' clump was partially stripped by ram pressure, creating a characteristic separation between dark matter and baryons similar to that seen in the Bullet Cluster. The Western 'stripped' clump fared worse: all of its gas was removed, strewn into the tidal debris of the Core and a faint trail of excess X-ray emission towards its current location where we find just dark matter and galaxies.

The smaller merger may have enabled a curious effect in the main, SE–NW merger. We postulate that gas in the Core was puffed up by the first collision, reducing ram-pressure stripping during the second. We also suggest that the main merger could have included two separate subclumps incident along a filament from the SE. The combined effect would be an enhancement of the 'slingshot' effect proposed by Owers et al. (2011), by which the subclumps' gas was accelerated ahead of their dark matter. This would explain the very large >35 arcsec observed separation between any gas ('ghostly' clump or NW interloper), galaxies and dark matter ('dark' clump), as well as the double-peaked morphology of the 'dark' clump. However, this scenario needs further confirmation.

The interpretation for this spectacular merging system will benefit immensely from additional observations and also from numerical simulations that can try to reproduce the new phenomenology shown in this cluster. The Western and Northwestern clumps have not been covered by *HST* observations and *Chandra* observations of the Western clump are shallow. Wide-field Subaru imaging in good seeing conditions and in several colours would also be useful to interpret the global environment. Numerical simulations should be performed to confirm the enhancement of the baryonic slingshot by the complicated merger configuration. The example of the Bullet Cluster has shown that the combination of complete lensing and X-ray observations (Markevitch et al. 2004; Bradač et al. 2006) with highly resolved hydrodynamical simulations (Springel & Farrar 2007; Randall et al. 2008) is a particularly powerful tool to understand the physics of merging clusters. In future work, we shall attempt to repeat this analysis on Abell 2744. The challenge laid down will be to explain the complicated phenomenology associated with this multiple merger, as well as to better constrain the collisional cross-section of dark matter, which our rough calculation suggests must be $\sigma/m < 3 \pm 1\,{\rm cm}^2\,{\rm g}^{-1}$, a tighter constraint than that from a similar analysis of the Bullet Cluster, which does not involve numerical simulations. Therefore, with our own numerical follow-ups we should be able to place similar or even better constraints than e.g. Randall et al. (2008) for the Bullet Cluster.

ACKNOWLEDGMENTS

The authors thank Matt Owers, Catherine Grant and Matthias Bartelmann for useful discussions. We are particularly grateful to

Douglas Clowe, the referee of this work, for his thorough reading of the manuscript. His competent comments and suggestions improved the quality of this work substantially. JM acknowledges financial support from the Heidelberg Graduate School of Fundamental Physics (HGSFP) and by contract research Galaxy Clusters of the Baden-Würrtemberg Stiftung. All runtime-expensive calculations were performed on dedicated GPU-machines at the Osservatorio Astronomico di Bologna. DC and RD acknowledge partial financial support from grant *HST*-GO-11689.09-A. RD also acknowledges support from NASA Grant NNH10CD19C. RM is supported by STFC Advanced Fellowship #PP/E006450/1 and ERC grant MIRG-CT-208994. ESC and LSJ acknowledge support from FAPESP (process ID 2009/07154) and CNPq. NB and YJ-T acknowledge support from the Spanish MICINN grant AYA2010-22111-C03-00 and from the Junta de Andalucía Proyecto de Excelencia NBL2003. MM and JM acknowledge financial support from ASI (contracts I/064/08/0, I/009/10/0 and EUCLID-IC) and from PRIN INAF 2009. This research was carried out in part at the Jet Propulsion Laboratory, California Institute of Technology, under a contract with NASA.

REFERENCES

Allen S. W., 1998, MNRAS, 296, 392
Anders E., Grevesse N., 1989, Geochim. Cosmochim. Acta, 53, 197
Andersson K. E., Madejski G. M., 2004, ApJ, 607, 190
Arnaud K. A., 1996, 101, 17
Ascasibar Y., Markevitch M., 2006, ApJ, 650, 102
Bartelmann M., Schneider P., 2001, Phys. Rep., 340, 291
Benítez N., 2000, ApJ, 536, 571
Bialek J. J., Evrard A. E., Mohr J. J., 2002, ApJ, 578, L9
Bond J. R., Cole S., Efstathiou G., Kaiser N., 1991, ApJ, 379, 440
Boschin W., Girardi M., Spolaor M., Barrena R., 2006, A&A, 449, 461
Bradač M., Schneider P., Lombardi M., Erben T., 2005, A&A, 437, 39
Bradač M. et al., 2006, ApJ, 652, 937
Bradač M., Allen S. W., Treu T., Ebeling H., Massey R., Morris R. G., von der Linden A., Applegate D., 2008, ApJ, 687, 959
Bradač M. et al., 2009, ApJ, 706, 1201
Braglia F., Pierini D., Böhringer H., 2007, A&A, 470, 425
Braglia F. G., Pierini D., Biviano A., Böhringer H., 2009, A&A, 500, 947
Bridle S. L., Kneib J., Bardeau S., Gull S. F., 2002, in Natarajan P., ed., Proc. Yale Cosmology Workshop, The Shapes of Galaxies and Their Dark Halos. World Scientific, Singapore, p. 38
Broadhurst T. et al., 2005, ApJ, 621, 53
Carrasco E. R. et al., 2010, ApJ, 715, L160
Clowe D., Gonzalez A., Markevitch M., 2004, ApJ, 604, 596
Clowe D., Bradač M., Gonzalez A. H., Markevitch M., Randall S. W., Jones C., Zaritsky D., 2006, ApJ, 648, L109
Coe D., Benítez N., Sánchez S. F., Jee M., Bouwens R., Ford H., 2006, AJ, 132, 926
Couch W. J., Newell E. B., 1984, ApJS, 56, 143
Cypriano E. S., Sodré L., Jr, Kneib J., Campusano L. E., 2004, ApJ, 613, 95
Czoske O., Moore B., Kneib J., Soucail G., 2002, A&A, 386, 31
Díaz-Giménez E., Zandivarez A., Proctor R., Mendes de Oliveira C., Abramo L. R., 2011, A&A, 527, A129
Dickey J. M., Lockman F. J., 1990, ARA&A, 28, 215
Dupke R. A., Bregman J. N., 2001a, ApJ, 562, 266
Dupke R. A., Bregman J. N., 2001b, ApJ, 547, 705
Dupke R. A., Bregman J. N., 2006, ApJ, 639, 781
Dupke R. A., Mirabal N., Bregman J. N., Evrard A. E., 2007, ApJ, 668, 781
Erben T., Van Waerbeke L., Bertin E., Mellier Y., Schneider P., 2001, A&A, 366, 717
Evrard A. E., Metzler C. A., Navarro J. F., 1996, ApJ, 469, 494
Feng J. L., Kaplinghat M., Yu H., 2010, Phys. Rev. Lett., 104, 151301
Finoguenov A., Sarazin C. L., Nakazawa K., Wik D. R., Clarke T. E., 2010, ApJ, 715, 1143
Giacintucci S. et al., 2008, A&A, 486, 347
Giovannini G., Tordi M., Feretti L., 1999, Nat, 4, 141
Girardi M., Mezzetti M., 2001, ApJ, 548, 79
Govoni F., Enßlin T. A., Feretti L., Giovannini G., 2001a, A&A, 369, 441
Govoni F., Feretti L., Giovannini G., Böhringer H., Reiprich T. H., Murgia M., 2001b, A&A, 376, 803
Grant C., 2001, ACIS Memo 195, space.mit.edu/ACIS/ps_files/ps195.ps.gz
Hallman E. J., Markevitch M., 2004, ApJ, 610, L81
Hayashi E., White S. D. M., 2006, MNRAS, 370, L38
Hoekstra H., 2007, MNRAS, 379, 317
Inogamov N. A., Sunyaev R. A., 2003, Astron. Lett., 29, 791
Jee M. J., Blakeslee J. P., Sirianni M., Martel A. R., White R. L., Ford H. C., 2007a, PASP, 119, 1403
Jee M. J. et al., 2007b, ApJ, 661, 728
Kaiser N., Squires G., Broadhurst T., 1995, ApJ, 449, 460
Kempner J. C., David L. P., 2004, MNRAS, 349, 385
Khosroshahi H. G., Ponman T. J., Jones L. R., 2007, MNRAS, 377, 595
Koekemoer A. M., Fruchter A. S., Hook R. N., Hack W., 2002, in Arribas S., Koekemoer A., Whitmore B., eds, The 2002 *HST* Calibration Workshop: *Hubble* After the Installation of the ACS and the NICMOS Cooling System. Space Telescope Science Institute, Baltimore, MD, p. 337
Krist J., 2003, Instrument Science Report ACS 2003-06
Lacey C., Cole S., 1993, MNRAS, 262, 627
Leauthaud A. et al., 2007, ApJS, 172, 219
Lee J., Komatsu E., 2010, ApJ, 718, 60
Mahdavi A., Hoekstra H., Babul A., Balam D. D., Capak P. L., 2007, ApJ, 668, 806
Markevitch M., Vikhlinin A., 2007, Phys. Rep., 443, 1
Markevitch M., Gonzalez A. H., David L., Vikhlinin A., Murray S., Forman W., Jones C., Tucker W., 2002, ApJ, 567, L27
Markevitch M., Gonzalez A. H., Clowe D., Vikhlinin A., Forman W., Jones C., Murray S., Tucker W., 2004, ApJ, 606, 819
Massey R., 2010, MNRAS, 409, L109
Massey R., Rhodes J., Leauthaud A., Capak P., Ellis R., Koekemoer A., Réfrégier A., Scoville N., 2007, ApJS, 172, 239
Massey R., Stoughton C., Leauthaud A., Rhodes J., Koekemoer A., Ellis R., Shaghoulian E., 2010, MNRAS, 401, 371
Mastropietro C., Burkert A., 2008, MNRAS, 389, 967
Mathis H., Lavaux G., Diego J. M., Silk J., 2005, MNRAS, 357, 801
Meneghetti M., Rasia E., Merten J., Bellagamba F., Ettori S., Mazzotta P., Dolag K., Marri S., 2010a, A&A, 514, A93
Meneghetti M., Fedeli C., Pace F., Gottlöber S., Yepes G., 2010b, A&A, 519, A90
Meneghetti M., Fedeli C., Zitrin A., Bartelmann M., Broadhurst T., Gottlöber S., Moscardini L., Yepes G., 2011, A&A, 530, A17
Merten J., Cacciato M., Meneghetti M., Mignone C., Bartelmann M., 2009, A&A, 500, 681
Million E. T., Allen S. W., 2009, MNRAS, 399, 1307
Milosavljević M., Koda J., Nagai D., Nakar E., Shapiro P. R., 2007, ApJ, 661, L131
Miralda Escudé J., 2002, ApJ, 564, 60
Morrison R., McCammon D., 1983, ApJ, 270, 119
Okabe N., Umetsu K., 2008, PASJ, 60, 345
Okabe N., Takada M., Umetsu K., Futamase T., Smith G. P., 2010a, PASJ, 62, 811
Okabe N., Okura Y., Futamase T., 2010b, ApJ, 713, 291
Owers M. S., Randall S. W., Nulsen P. E. J., Couch W. J., David L. P., Kempner J. C., 2011, ApJ, 728, 27
Pavlovsky C. e. A., 2006, Technical Report, Advanced Camera for Surveys Instrument Handbook. Version 7.1. STScI, Baltimore
Pawl A., Evrard A. E., Dupke R. A., 2005, ApJ, 631, 773
Randall S. W., Markevitch M., Clowe D., Gonzalez A. H., Bradač M., 2008, ApJ, 679, 1173
Rhodes J., Refregier A., Groth E. J., 2000, ApJ, 536, 79
Rhodes J. D. et al., 2007, ApJS, 172, 203
Russell H. R., Sanders J. S., Fabian A. C., Baum S. A., Donahue M.,

Edge A. C., McNamara B. R., O'Dea C. P., 2010, MNRAS, 406, 1721
Sanders J. S., Fabian A. C., Smith R. K., Peterson J. R., 2010, MNRAS, 402, L11
Sanders J. S., Fabian A. C., Smith R. K., 2011, MNRAS, 410, 1797
Sarazin C. L., 2004, J. Korean Astron. Soc., 37, 433
Shan H., Qin B., Fort B., Tao C., Wu X., Zhao H., 2010, MNRAS, 406, 1134
Smail I., Ellis R. S., Dressler A., Couch W. J., Oemler A., Jr, Sharples R. M., Butcher H., 1997, ApJ, 479, 70
Smith R. K., Brickhouse N. S., Liedahl D. A., Raymond J. C., 2001, ApJ, 556, L91
Springel V., Farrar G. R., 2007, MNRAS, 380, 911
Sunyaev R. A., Norman M. L., Bryan G. L., 2003, Astron. Lett., 29, 783
Tucker W. et al., 1998, ApJ, 496, L5
Umetsu K., Medezinski E., Broadhurst T., Zitrin A., Okabe N., Hsieh B., Molnar S. M., 2010, ApJ, 714, 1470
Vikhlinin A. et al., 2009, ApJ, 692, 1060
Williams L. L. R., Saha P., 2011, MNRAS, 415, 448
Zhang Y., Finoguenov A., Böhringer H., Ikebe Y., Matsushita K., Schuecker P., 2004, A&A, 413, 49
Zitrin A. et al., 2009, MNRAS, 396, 1985
Zitrin A. et al., 2010, MNRAS, 408, 1916
Zitrin A., Broadhurst T., Coe D., Liesenborgs J., Benítez N., Rephaeli Y., Ford H., Umetsu K., 2011a, MNRAS, 413, 1753
Zitrin A., Broadhurst T., Bartelmann M., Rephaeli Y., Oguri M., Benítez N., Hao J., Umetsu K., 2011b, preprint (arXiv e-prints)
Zitrin A. et al., 2011c, preprint (arXiv:1103.5618)
Zitrin A., Broadhurst T., Barkana R., Rephaeli Y., Benítez N., 2011d, MNRAS, 410, 1939
Zu Hone J. A., Lamb D. Q., Ricker P. M., 2009a, ApJ, 696, 694
Zu Hone J. A., Ricker P. M., Lamb D. Q., Karen Yang H., 2009b, ApJ, 699, 1004

This paper has been typeset from a TEX/LATEX file prepared by the author.